UCLA
UCLA Previously Published Works

Title

Anisotropic 2D van der Waals Magnets Hosting 1D Spin Chains

Permalink

https://escholarship.org/uc/item/65x574jp

Journal

Advanced Materials, 36(31)

ISSN

0935-9648

Authors

Park, Eugene

Philbin, John P

Chi, Hang

et al.

Publication Date

2024-08-01

DOI

10.1002/adma.202401534

Copyright Information

Peer reviewed

Anisotropic 2D van der Waals Magnets Hosting 1D Spin Chains

Eugene Park,* John P. Philbin, Hang Chi, Joshua J. Sanchez, Connor Occhialini,
Georgios Varnavides, Jonathan B. Curtis, Zhigang Song, Julian Klein,
Joachim D. Thomsen, Myung-Geun Han, Alexandre C. Foucher, Kseniia Mosina,
Deepika Kumawat, N. Gonzalez-Yepez, Yimei Zhu, Zdeněk Sofer, Riccardo Comin,
Jagadeesh S. Moodera, Prineha Narang, and Frances M. Ross*

The exploration of 1D magnetism, frequently portrayed as spin chains, constitutes an actively pursued research field that illuminates fundamental principles in many-body problems and applications in magnonics and spintronics. The inherent reduction in dimensionality often leads to robust spin fluctuations, impacting magnetic ordering and resulting in novel magnetic phenomena. Here, structural, magnetic, and optical properties of highly anisotropic 2D van der Waals antiferromagnets that uniquely host spin chains are explored. First-principle calculations reveal that the weakest interaction is interchain, leading to essentially 1D magnetic behavior in each layer. With the additional degree of freedom arising from its anisotropic structure, the structure is engineered by alloying, varying the 1D spin chain lengths using electron beam irradiation, or twisting for localized patterning, and spin textures are calculated, predicting robust stability of the antiferromagnetic ordering. Comparing with other spin chain magnets, these materials are anticipated to bring fresh perspectives on harvesting low-dimensional magnetism.

1. Introduction

A unique feature enabled by 1D magnetism is the ability to utilize magnetism in individual spin chains. This is made possible by separating the magnetic chains in the structure by a sufficient distance such that there are minimal interactions between neighboring chains. Unique physics and capability are anticipated to arise from this platform that may address the limitations of conventional magnetic materials by facilitating magnetic manipulation without unwanted interactions between spins. Such low-dimensional quantum spin systems have primarily been studied in bulk materials with well-separated 1D spin chains. The resulting exotic 1D physics includes Bose–Einstein condensation behavior in $TlCuCl_3$ with spin ladders, the spin-Peierls

E. Park, J. Klein, J. D. Thomsen, A. C. Foucher, F. M. Ross
Department of Materials Science and Engineering
Massachusetts Institute of Technology
Cambridge, MA 02139, USA
E-mail: eugenep@mit.edu; fmross@mit.edu
J. P. Philbin, J. B. Curtis, J. D. Thomsen, P. Narang
College of Letters and Science
University of California
Los Angeles, CA 90095, USA
H. Chi, J. S. Moodera
Francis Bitter Magnet Laboratory
Plasma Science and Fusion Center
Massachusetts Institute of Technology
Cambridge, MA 02139, USA

H. Chi
Department of Physics
University of Ottawa
Ottawa, ON K1N 6N5, Canada
H. Chi
Nexus for Quantum Technologies
University of Ottawa
Ottawa, ON K1N 6N5, Canada
J. J. Sanchez, C. Occhialini, D. Kumawat, N. Gonzalez-Yepez, R. Comin,
J. S. Moodera
Department of Physics
Massachusetts Institute of Technology
Cambridge, MA 02139, USA
G. Varnavides
Miller Institute for Basic Research in Science
University of California
Berkeley, CA 94720, USA
G. Varnavides
National Center for Electron Microscopy
Molecular Foundry
Lawrence Berkeley National Laboratory
Berkeley, CA 94720, USA

transition in vanadate family compounds such as α'-NaV$_2$O$_5$ with zigzag spin chains, and ferrotoroidicity hosted in Ba$_6$Cr$_2$S$_{10}$ with its dimerized antiferromagnetic spin chain structure.[1–4] Low-dimensional quantum spin systems can also be studied by synthesizing isolated chains individually, for example, by terrace or step-flow growth on a nonmagnetic substrate[5,6] or by precise placement of individual magnetic atoms on a surface using spin-resolved scanning tunneling microscopy.[7–9] However, these strategies are less suited for executing seamless integration with other materials, as needed for realizing diverse functionalities and incorporating into devices designed to harness the materials' distinctive magnetic properties.

Recent revelations of intrinsic magnetism in 2D van der Waals (vdW) materials have opened opportunities for studying and utilizing new types of low-dimensional magnetic materials.[10,11] A key benefit of 2D materials is that their planar nature enables easy integration with other materials for functionality, and well-controlled large-scale synthesis may be possible.[12,13] 2D vdW magnets may therefore address the constraints that limit studies and applications based on both bulk spin chain materials and individually synthesized 1D magnetic chains. However, most 2D materials possess a symmetric honeycomb structure within each layer, which for magnetic materials such as the well-known MPS$_3$ family,[10,11] with M a transition metal, leads to spin communication in multiple directions. This symmetry poses challenges in controlling individual magnetic characteristics independently, and leads to crosstalk in spins. As a result, the implementation of magnetic applications sensitive to such interactions is restricted. This motivates exploration into new types of 2D magnets that combine the benefits of the extreme anisotropy of isolated spin chains with the advantages of a vdW crystal structure for planar integration.

Here, we investigate 2D vdW magnets that show a pronounced anisotropy by virtue of a structure that contains well-separated intrinsic 1D spin chains. The materials under examination, AgCrP$_2$S$_6$ (ACPS) and AgVP$_2$S$_6$ (AVPS), referred to collectively as AgMP$_2$S$_6$ (AMPS) with M a transition metal, have layered structures with an antiferromagnetic (AFM) ground state that differ from those of the MPS$_3$ magnets in containing, within each layer, chains of M atoms separated by chains of Ag atoms.[14,15] Using scanning transmission electron microscopy (STEM), we describe a comprehensive atomistic characterization of the structures showing the alternating chains, and we combine this with measurements of the anisotropy of magnetic and optical behavior parallel and perpendicular to the spin chain direction in the plane of the 2D layers. We calculate the strength of magnetic exchange interactions to illustrate that each chain is effectively isolated within and between layers. Finally, we demonstrate a promising versatility in these materials, showing that the structure can be engineered in different ways to provide tunability for probing fundamental magnetism with reduced dimensionality. The atomistic engineering of anisotropic 2D magnets opens the door to magnetic applications in 1D magnetic phenomena and suggests the feasibility of practical utilization, highlighting the prospect of tapping into the characteristics of 1D magnetism at an applied level.

2. Results and Discussion

2.1. Structural Characterization of 2D Magnets with Separated 1D Chains

Figure 1 illustrates the highly anisotropic nature of the AMPS structure and compares it with that of the MPS$_3$ vdW magnets. The crystal structure of ACPS is displayed schematically in Figure 1a, while AVPS possesses similar structural features. The structure contains alternating zigzag chains composed of Cr and Ag atoms, separated by P and S, with Cr being the element that gives rise to magnetic order. Each layer has an offset parallel to the chain direction with a repeat every three layers. To illustrate this feature of the atomic arrangement, Figure 1a shows both the monolayer (1L) and trilayer (3L) structural models. The crystals are synthesized as described in the Experimental Section and illustrated in Figures S1 and S2 (Supporting Information). Bulk ACPS has a plate-like morphology and can be successfully exfoliated down to mono- to few layers. To examine the microstructure, we exfoliated few-layer electron-transparent flakes from the bulk crystal and transferred them onto transmission electron microscopy (TEM) grids (Experimental Section; Figures S3–S5, Supporting Information). In Figure 1b, we directly visualize the 1D chain structure in ACPS using aberration corrected STEM at 200 kV. The image intensity is approximately proportional to the projected atomic number squared, and therefore the brightest atoms visible are Ag, with Cr darker and located between the Ag chains, and P and S darker still and difficult to distinguish. Energy dispersive spectroscopy (EDS), however, shows the composition directly, confirming Cr between the Ag chains (Figure 1c). The alternating Ag and Cr chains are visualized in cross-sectional geometry in Figure 1f as well as in Figure S6 (Supporting Information).

The layered nature of ACPS is characterized in Figure 1e–g, where Figure 1e is a plan view image with different number of layers of ACPS at an edge of the flake. The cross-sectional STEM image in the crystallographic *b*-direction (Figure 1g) shows the stacking order that repeats every third layer. The cross-sectional images indicate no planar defects such as stacking faults within or between layers. The highly ordered stacking of ACPS and its apparently defect-free structure make it a suitable 2D vdW magnet for engineering low-dimensional magnetism. ACPS is not the only 2D magnet with 1D spin chains. AVPS, another 2D magnet with the same structure, is shown in plan view STEM in

Z. Song
John A. Paulson School of Engineering and Applied Sciences
Harvard University
Cambridge, MA 02139, USA

M.-G. Han, Y. Zhu
Condensed Matter Physics and Materials Science Department
Brookhaven National Laboratory
Upton, NY 11973, USA

K. Mosina, Z. Sofer
Department of Inorganic Chemistry
University of Chemistry and Technology Prague
Technická 5, Prague 166 28, Czech Republic

D. Kumawat
Department of Physics
Mount Holyoke College
South Hadley, MA 01075, USA

**ADVANCED
SCIENCE NEWS**

www.advancedsciencenews.com

**ADVANCED
MATERIALS**

www.advmat.de
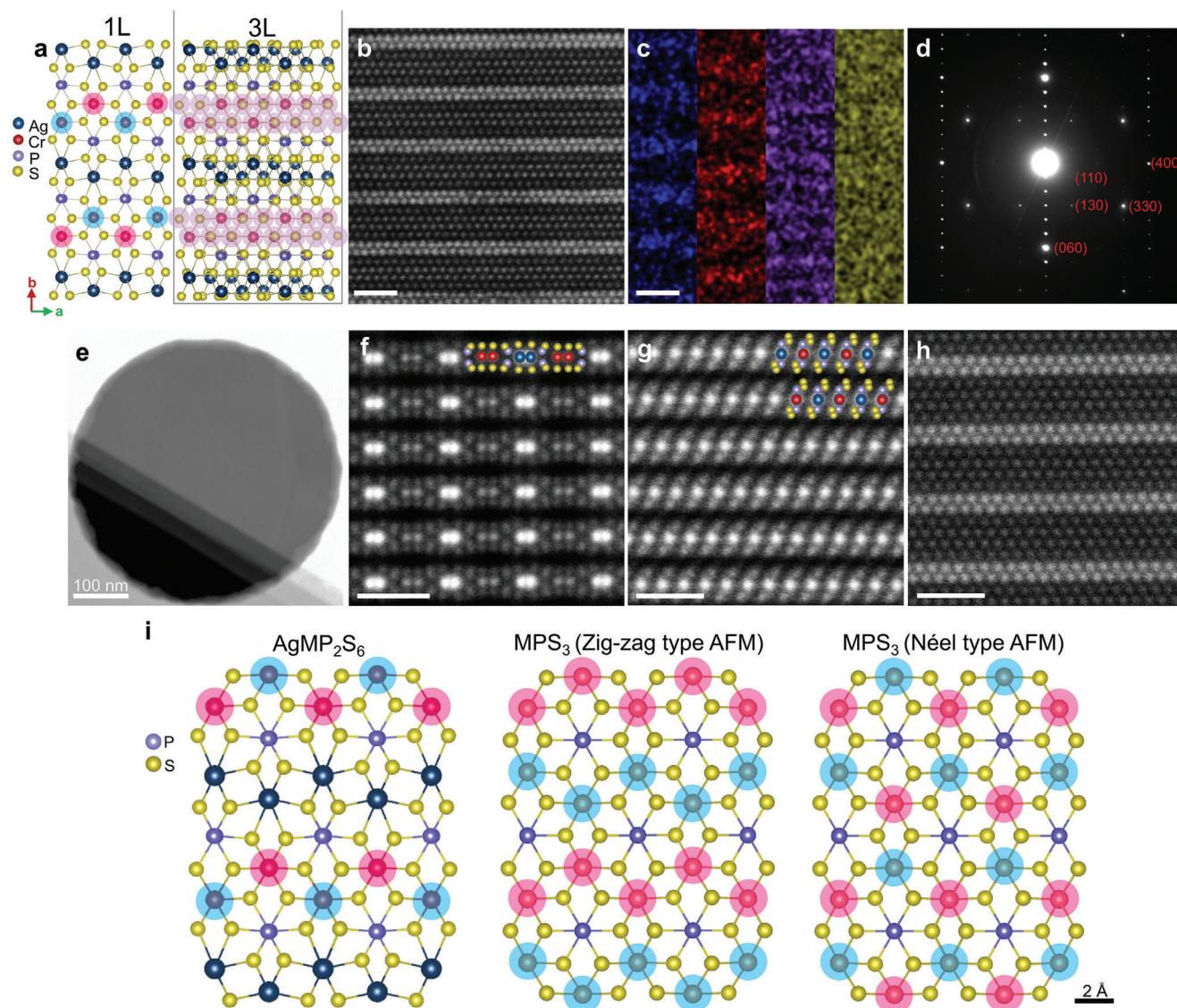
Figure 1. STEM structural characterization of 2D vdW magnets with 1D magnetic chains. a) Schematic of the structure of $AgCrP_2S_6$ shown for monolayer (1L) and trilayer (3L). Zigzag chains of Cr atoms are highlighted in blue (spin up) and pink (spin down) for 1L and in purple for 3L. b) Plan view STEM image of $AgCrP_2S_6$. c) EDS map of $AgCrP_2S_6$ where Ag, Cr, P, and S are indicated in blue, red, purple, and yellow, respectively. d) The diffraction pattern corresponding to the area shown in (b). e) Low magnification STEM image showing different layer numbers of the flake. f,g) STEM images of the cross-sections in the crystallographic *a*- and *b*-directions, respectively, with atomic structures overlaid. h) Plan view STEM image of $AgVP_2S_6$. Scale bars in (b), (c), and (f–h), 1 nm. i) Schematic comparing the structure of $AgMP_2S_6$ with two types of MPS_3 where M denotes the transition metal. Magnetic atoms are highlighted with blue (spin up) or pink (spin down) to visualize the spin arrangement.

Figure 1h. The key difference between these two materials is that the chromium atom in ACPS has half integer spin of $S = 3/2$,[14] while the vanadium atom in AVPS has an integer spin of $S = 1$ and the spin chain is known to have a Haldane gap.[16,17] With both Cr and V arranged in 1D spin chains, these different spin states provide an additional variable to study low-dimensional magnetism.

The arrangement of the M atoms in the AMPS structure is compared in Figure 1i to that in the MPS_3 magnets, in which the magnetic atoms reside on a honeycomb lattice with a zigzag or Néel type AFM arrangement. The occupancy of alternate rows of the AMPS structure by nonmagnetic Ag atoms, separating

out the magnetic atom locations in one direction, is expected to change the interaction between the spin chains in one in-plane direction, as we discuss below.

2.2. Magnetic Properties of 1D Spin Chains in ACPS

The significance of the 1D Cr chains is manifested in the highly anisotropic magnetization profiles of ACPS when an in-plane external magnetic field is applied along and perpendicular to the chain direction. This is illustrated in the vibrating sample magnetometry (VSM) measurements in **Figure 2a–c**. The

ADVANCED
SCIENCE NEWS
www.advancedsciencenews.com

ADVANCED
MATERIALS
www.advmat.de
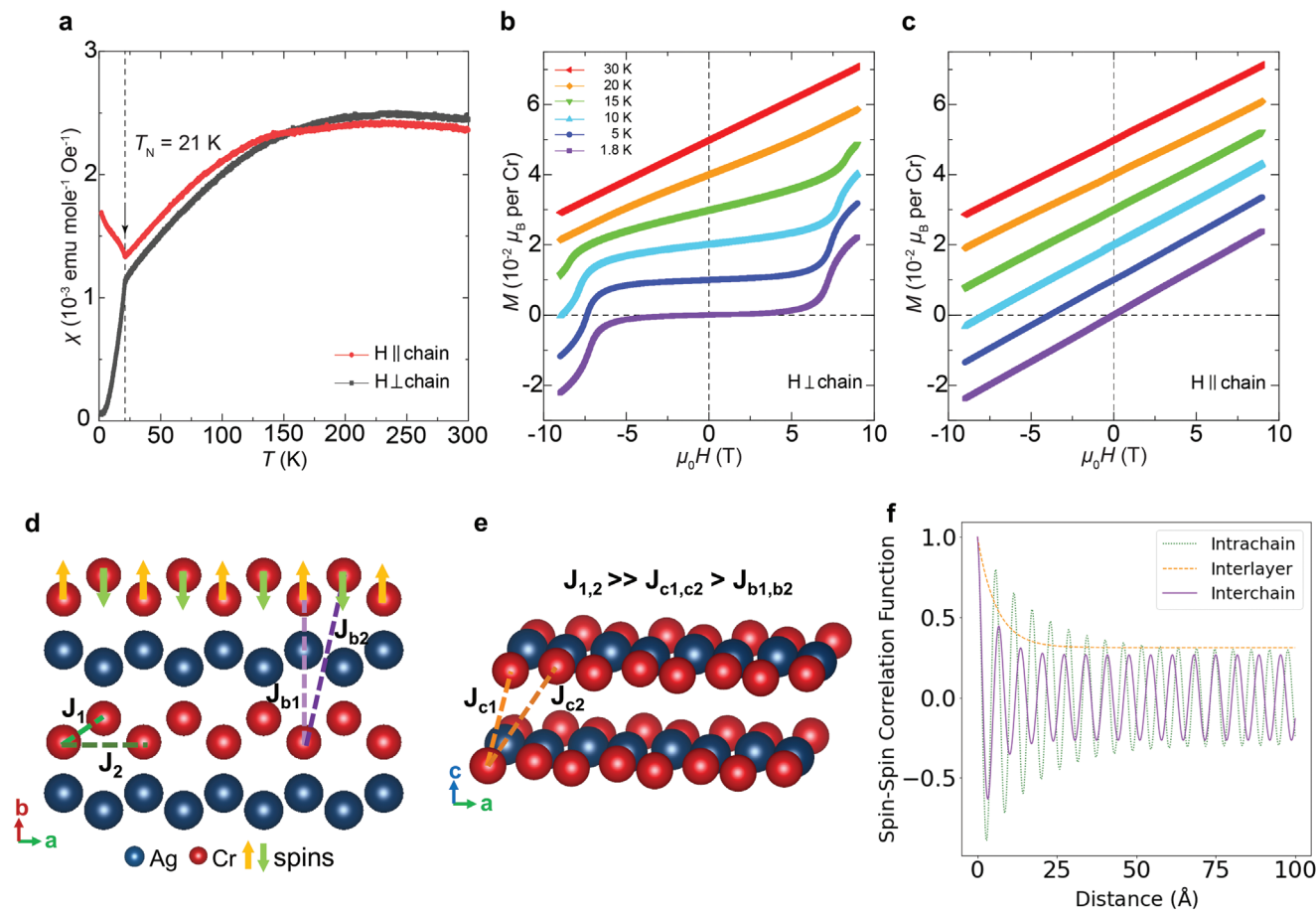
Figure 2. Magnetic properties of AgCrP$_2$S$_6$. a) Magnetic susceptibility (χ) measured as a function of temperature with external magnetic field applied ($\mu_0 H = 1$ T) along the crystallographic a- (red) and b- (black) directions, respectively. Black arrow indicates the Néel temperature $T_N = 21$ K. b) Magnetization (M) versus H perpendicular to the Cr chain (i.e., along the b-direction) and c) parallel to the Cr chain (a-direction) at selected temperatures. Curves are each vertically shifted by 1×10^{-2} μ_B per Cr for visual clarity. Schematic illustrations of ACPS (without P and S atoms for clarity) in d) plan view, and e) cross-sectional view (b-direction) where $J_1 = -3.91$ meV and $J_2 = 0.58$ meV denote the nearest and next nearest exchange couplings, $J_{b1} = -0.001345$ meV and $J_{b2} = -0.02615$ meV are interchain exchange couplings, and $J_{c1} = 0.1865$ meV and $J_{c2} = -0.0149$ meV are interlayer exchange couplings. Negative and positive signs denote AFM and FM couplings, respectively. f) Spin–spin correlation function for AgCrP$_2$S$_6$ just below T_N. The sinusoidal behavior indicates AFM coupling and the exponential decay indicates ferromagnetic coupling.

temperature dependence of magnetic susceptibility with an external field of 1 T applied along the a- and b-directions is shown in Figure 2a. In these data, the kink (labeled by a black arrow) reveals the Néel temperature (T_N). Below this temperature, anisotropic AFM ordering develops, while above T_N, largely isotropic paramagnetic behavior dominates in both directions. The observed T_N agrees well with our density functional theory (DFT) calculation results, discussed below, as well as with a previous literature value.[14] Below T_N, the anisotropy of the magnetic susceptibility implies that the easy axis is perpendicular to the chain, i.e., along the crystallographic b-axis. Above T_N, the broad maximum indicates that short-range antiferromagnetic order has formed far above T_N, which is a typical feature for low-dimensional systems.[18–20]

In Figure 2b, in the AFM state, the field-dependent magnetization $M(H)$ of ACPS displays a spin flop behavior with perpendicular magnetic field exceeding 7 T. This implies that the spins are arranged with antiferromagnetic ordering and is consistent with the easy b-axis being perpendicular to the chain. Along the

magnetically hard a-axis, magnetization increases linearly with H in Figure 2c. However, within the field range investigated of up to 9 T, the magnitude of magnetization is quite small, on the order of 10^{-2} Bohr magneton μ_B per Cr ion. To access the field-induced AFM–ferromagnetic spin-flip transition, a higher magnetic field would be required. This suggests that the AFM ordering of each 1D spin chain is stable and unaffected by neighboring spin chains, consistent with their wide spacing. This constitutes a difference in magnetic properties compared to the Néel or zigzag type AFM configurations often seen in MPX$_3$ compounds with honeycomb structure and shown in Figure 1i. It has been reported[20] that the spin-flip transition field is higher for zigzag type AFM structures (second panel), which have some anisotropy in the ab-plane, compared to Néel type AFM (third panel).[20] ACPS (first panel) fits this pattern with an even higher spin-flip transition field and anisotropy.

These experimental results agree with DFT + U calculations performed using Siesta-TB2J,[21,22] where the lowest energy ground state is AFM with an easy axis perpendicular to the

**ADVANCED
SCIENCE NEWS**

www.advancedsciencenews.com

**ADVANCED
MATERIALS**

www.advmat.de
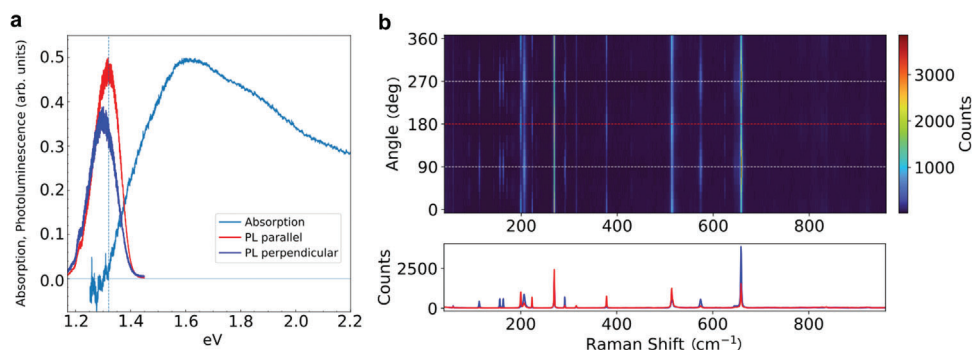
Figure 3. Optical properties of $AgCrP_2S_6$. a) Photoluminescence (PL) and absorption measurements at $T = 300$ K. Dashed line indicates DFT-calculated bandgap of $E = 1.32$ eV. Red PL traces correspond to incident photon polarization aligned parallel, and blue perpendicular, to the chain axis. The kink in the PL near 1.22 eV is an artifact of the grating. b) Raman spectra in the XX channel at $T = 5$ K. Zero degrees corresponds to the chain axis. Red dashed lines indicate angles parallel, and blue perpendicular, to the chain axis.

Cr-chain direction. Furthermore, DFT results indicate that the AFM ground state is mainly dependent on the intrachain nearest- and next-nearest neighbor exchange coupling values (J_1, J_2). The schematic in Figure 2d indicates the major magnetic interactions of Cr atoms, with Ag shown to emphasize the spacing between Cr chains. Interlayer exchange coupling ($J_{c1,2}$) values are small and negative, leading to ferromagnetic (FM) coupling between layers. Interchain exchange couplings ($J_{b1,2}$) are two orders of magnitude smaller than the nearest-neighbor exchange coupling values. The interchain interaction is orders of magnitude smaller than that of MPX_3 compounds (Table S1, Supporting Information).[23] Thus, ACPS effectively hosts a 1D spin system.

The relationship between the magnetic state and the intra-chain, interchain, and interlayer exchange couplings is further studied via the correlation function. Figure 2f presents an example spin–spin correlation function of ACPS just below T_N, showing that the AFM nature of intrachain coupling and the correlation lengths are intertwined. These calculations reveal that the magnetic order is first established by intrachain, then interlayer, and finally interchain correlations. An interesting outcome is that the interchain correlation is the hardest to establish; all interchain correlation is lost rapidly on increasing the temperature above T_N (Figure S7, Supporting Information).

2.3. Optical Characterization of ACPS

We next discuss the electronic bandgap of ACPS which we explore through DFT calculations. The calculations reveal flat bands with a small dispersion and an indirect gap of 1.32 eV (Figure S8, Supporting Information). Because of the flat bands it is likely that the gap will behave like a direct gap. In order to test these calculations, we measured the bandgap of ACPS using optical absorption and photoluminescence (PL) measurements at room temperature (**Figure 3a**). The PL spectra, recorded using a 532 nm laser, display a peak near $E = 1.32$ eV, which varies slightly for incident photon polarization along or transverse to the chain axis, demonstrating the electronic anisotropy of the material. Optical transmissivity (T) and reflectivity (R) measurements were performed with a halogen lamp (see the Experimental Section). The resulting absorption ($A = 1 - T - R$) indicates an absorption threshold near $E = 1.32$ eV. These results are in excellent

agreement with the DFT bandgap (dashed line) and suggest that ACPS is a direct bandgap semiconductor. Furthermore, Raman spectroscopy, performed at $T = 5$ K for a range of linear polarization incident angles, reveals the highly anisotropic character of ACPS (Figure 3b; cross-polarization data presented in Figure S9 in the Supporting Information). Numerous peaks originate from the large unit cell with 10 distinct atomic sites, and can all be attributed to phonons. We observed no additional peaks when compared to data taken above T_N (Figure S10, Supporting Information), indicating that the magnetic order is locked to the same symmetry as the lattice.

2.4. Atomistic Engineering of 1D Spin Chain Layered Magnets

We now turn to the engineering of these 2D magnets through different approaches: alloying and imposing additional structural features. We expect such engineering to enable interesting opportunities for manipulating spin textures for device applications, as these unique and highly anisotropic materials offer an extra degree of freedom to work with 1D magnetism.[24] We first introduce an example alloy, then show two strategies for patterning.

In **Figure 4a**, we show the alloy $AgCr_{0.5}V_{0.5}P_2S_6$ (ACVPS), synthesized in the same way as ACPS and AVPS (Figures S1, S2, and S11 (Supporting Information), Experimental Section). In this example of the feasibility of alloy design, the magnetic atoms along the chains have mixed spin states with half-integer spin for Cr and integer spin for V. By alloying the metal of the magnetic chains or the metal of the nonmagnetic stripes, we expect to tune, respectively, the J values in the a- and b-directions independently. Alloying has already uncovered significant physics in MPS_3 magnets,[20] but the ability to tune the exchange interactions in the desired orientation is not available in the MPS_3 structure. In materials with high structural anisotropy, the opportunities for accessing new physics could be even greater. Mixed spin state Heisenberg AFM chains are expected to have a ferrimagnet ground state according to the Lieb–Mattis theorem,[25] different spin correlation dynamics, as well as a change in the effective spin state.[26] Such mixed spin systems are accessible in conventional bulk materials[26,27] but are yet to be explored in the 2D vdW materials system. Alloys such as that shown in Figure 4
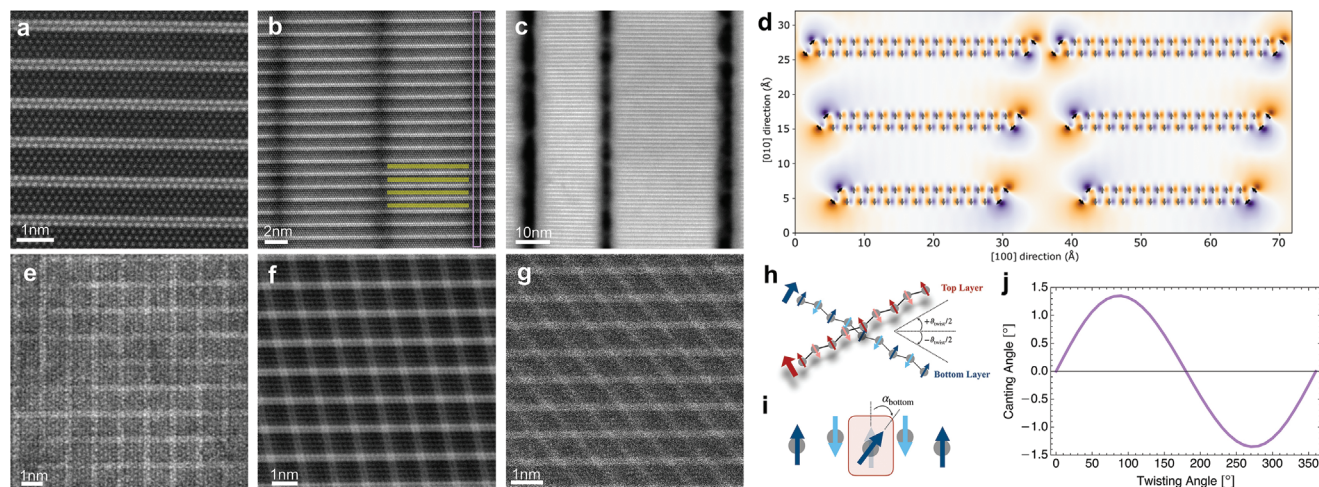
Figure 4. Atomistic engineering of 1D spin chains. a) Plan view STEM image of $AgCr_{0.5}V_{0.5}P_2S_6$. b) STEM image of 40 nm thick $AgCrP_2S_6$ where black vertical regions such as that outlined in purple are irradiated with the electron beam to create short chains about 7 nm in length (highlighted in yellow). Scale bar, 2 nm. c) STEM image with varying chain lengths and with increased electron beam exposure times. d) Magnetic vector potential contribution along the beam direction projected along [001], for varying-length magnetic chains using an idealized surface AFM ordering (black arrows). e) STEM image of two ≈10 nm thick $AgCrP_2S_6$ flakes stacked with a high twist angle of ≈90°, f) STEM image of two ≈25 nm thick stacked $AgVP_2S_6$ flakes, and g) stacked ≈15 and ≈50 nm thick $AgCr_{0.5}V_{0.5}P_2S_6$ flakes. h) Schematic of the chain system considered. Relative twist is referenced with respect to the lab frame. i) Canting angle for the spin at the intersection of the two chains is defined with respect to zero canting angle lying along the easy axis. j) Canting angle as a function of the applied twist angle, displaying a maximum (but still small) value when the chains are orthogonal.

may therefore be promising candidates to access mixed spin state physics.

In Figure 4b,c, we change the structure of ACPS by controlling the length of the Cr spin chains. This was accomplished by irradiation of an ≈40 nm thick ACPS crystal with the focused electron beam in STEM. Electron beam irradiation causes knock-on damage that cuts through the crystal, leaving a few nanometers transition region at the newly formed surfaces. The gap between the segmented chains can also be controlled. In Figure 4b, we see that some material remains in the gaps; higher doses create slits through the crystal, although with collateral surface damage (Figure 4c). The electron beam therefore separates the chains into segments but also causes surface restructuring and amorphization at the chain ends. The use of irradiation to create magnetic chains is expected to be most controllable through use of thinner crystals where the required dose is lower.

We expect the spins of surface Cr atoms to cant, in order to accommodate the loss of symmetry, giving rise to surface AFM ordering.[28] Depending on the nature of this surface-spin canting, the resulting spin configurations may develop a total magnetic moment, with benefits for all-spin-based devices. To investigate whether 1D spin chains are magnetically isolated from one another, we calculate the projected magnetic vector potential for two model surface-spin orientations and varying chain spacings (Figure 4d and Figure S12 (Supporting Information)). We find that the spin signatures are fairly robust to varying spin chain separations which, in combination with the weak interchain couplings discussed above, suggest that the 1D chains can be treated as magnetically isolated. Figure 4d also highlights that the nature of the surface-spin canting should be visible in projection, and in principle observable with a recently developed simultaneous ptychographic reconstruction framework (Figure S13, Supporting Information).[29]

We next discuss interface engineering of the 2D magnets, highlighting the versatility in enabling exotic phenomena due to new states arising from the interlayer interactions ($J_{interlayer}$). With a large $J_{interlayer}$, new phases are expected to arise at the interface, while with weak $J_{interlayer}$, the layers should not interact but rather maintain their unique properties. Although both cases are of interest, the first is more commonly studied,[30] yet the properties of ACPS and AVPS should allow investigation of the second. Figure 4e–g demonstrates that ACPS, AVPS, and ACVPS can be stacked with a controllable angle to result in structures with 1D spin chains propagating in different directions. The strong crystal anisotropy and weak interlayer exchange coupling predict that the spin chains in each stack are isolated from each other with minimal canting angle at the center of rotation. To predict changes in canting angle due to the stacking, we used a simple model (Experimental Section). We assume single chains in the top and bottom layers are rotated with an angle, as shown in Figure 4h, then minimize the energy as a function of the twist angle ϑ to obtain the local spin angle on each site. This is then referenced to its value if the chains were uncoupled, which would be along the easy axis and antialigned with its neighbors, as depicted in Figure 4i. This canting angle α is plotted in Figure 4j as a function of the twist angle. We see it is generically quite small, but is maximal when the two chains are orthogonal as this applies the largest effective torque on the spin at the center. We can also model the dependence of the canting angle on the strength of the interlayer exchange interaction, shown in Figure S14 (Supporting Information) for a variety of interlayer coupling strengths. We observe that the canting angle becomes larger with stronger interlayer coupling, as the spin is only incentivized to cant due to the exchange torque from the neighboring layer. It is interesting to note that the canting angle also acquires a more nonlinear dependence on the twist angle, showing nonsinusoidal

**ADVANCED
SCIENCE NEWS**

www.advancedsciencenews.com

**ADVANCED
MATERIALS**

www.advmat.de

dependence. Physically, the interlayer exchange coupling is expected to be highly sensitive to strain, since it involves tunneling across the vdW gap and depends exponentially on the interlayer distance, which may change upon straining. Experimental data on the magnetic properties of these engineered chain structures would be needed to verify these predictions and explore opportunities arising from stacked 1D chain vdW magnets.

3. Conclusion

We have demonstrated several material candidates as a new class of 2D vdW magnets that host highly anisotropic 1D chains of magnetic atoms. These 2D vdW materials with well-separated 1D spin chains enable new possibilities for tuning and exploiting magnetism at low dimension and extending the range of 2D magnet research, for example, as a platform for studying the Luttinger liquid phase of half integer spin 1D Heisenberg chains.[31] Another direction of great interest is as a system to study magnon diffusion, since the 1D chains of magnetic atoms may act as a spin wave guide.[32,33] We have also established a framework for structural engineering of these materials to enable future exploration of additional opportunities. A 1D chain structure with tailored chain lengths presents an intriguing opportunity for realizing atomic scale all-spin-based devices such as spin logic gates, if we imagine using the magnetic chains for input/output interconnects. 1D chains in a twisted configuration may enable influencing of magnon transport through disruption by the top or bottom layer spin chains. Further chemical and compositional engineering in this family of materials offers exciting prospects for fundamental exploration of magnetism and for tailor-designed spintronic devices that utilize their unique anisotropic properties.

4. Experimental Section

Chemical Vapor Transport: Synthesis of thiophosphates was performed by direct reaction from elements using powder silver (−325 mesh, 99.9%, Strem, USA), vanadium (−325 mesh, 99.7%, Strem, USA), chromium (−60 mesh, 99.99%, Chemsavers, USA), sulfur (1–3 mm, 99.9999%, Wuhan Xinrong New Materials, China), phosphorus (1–6 mm, 99.9999%, Wuhan Xinrong New Materials, China), and iodine as a transport medium (99.9%, Fisher Scientific, Czech Republic). The elements in stochiometric ratio corresponding to 15 g of crystal were placed in an ampoule using 1 at% excess of sulfur and phosphorus together with iodine (3 mg mL^{-1}). The ampoule (35 × 200 mm) was melt sealed by oxygen–hydrogen torch under a base pressure of 1×10^{-3} Pa. The sealed ampoule was first placed horizontally in muffle furnace and heated on 450 °C for 50 h, on 500 °C for 50 h, and at 600 °C for 50 h with a heating and cooling rate of 1 °C min^{-1}. After complete reaction of elements, the ampoule was mechanically homogenized and placed in a horizontal two zone furnace. First, the growth zone was heated at 750 °C, while source zone was kept at 500 °C for 50 h to clean growth zone. Subsequently, the thermal gradient was reversed and source zone was kept at 700 °C and growth zone at 600 °C for 14 days. Finally, the furnace was cooled to room temperature while the ampoule was opened in a glove box.

X-Ray Diffraction (XRD): Powder XRD data were collected under ambient conditions on a Bruker D8 Discoverer (Bruker, Germany) powder diffractometer with parafocusing Bragg–Brentano geometry using CuK$_\alpha$ radiation ($\lambda = 0.15418$ nm, $U = 40$ kV, $I = 40$ mA). Data were scanned over the angular range 10°–70° (2θ) with a step size of 0.019° (2θ). The acquired data were analyzed using the HighScore Plus 3.0 software.

Sample Fabrication: Samples were mechanically exfoliated onto SiO$_2$/Si wafers. Sample thickness was verified using optical contrast and

atomic force microscopy measurement. Each sample was then transferred on to a SiN$_x$ TEM grid using cellulose acetate butyrate as the polymer handle for transfer.

Scanning Transmission Electron Microscopy: A probe-corrected Thermo Fischer Scientific Themis Z G3 was operated at 200 kV with a probe current of 20 pA and convergence semiangle of 18.9 mrad. The frame size was 1024 × 1024 with a dwell time of 500 ns per pixel. Velox software was used to overlap 10–15 images to increase signal to noise ratio and correct drift. For fabricating short chains, the electron beam was focused on to a rectangular area and the beam current was increased to 50 pA to irradiate the area of interest for 60–90 s.

Vibrating Sample Magnetometry: Temperature, field, and angle-dependent magnetic properties were measured in a Quantum Design Physical Property Measurement System equipped with a 9 T superconducting magnet. An external magnetic field of 1 T was applied for the magnetization versus temperature measurement in the temperature range of 1.8–300 K.

Optical Measurements: PL and Raman spectroscopy measurements were performed in a Montana Instruments closed-cycle optical cryostat. Experiments were performed in a backscattering geometry using a confocal microscope spectrometer (Horiba LabRAM HR Evolution) with a 20× (PL) or 50× (Raman) objective (Olympus) and 532 nm laser excitation at a power of 100 µW. Scattered light was dispersed by an 1800 lines mm^{-1} grating and detected with a liquid nitrogen cooled charge-coupled device camera. The spectrometer integration time was 2 min and each scan was taken twice and then averaged before analysis. Polarized Raman and PL spectra were recorded with a linearly polarized incident beam. For angle-resolved polarized Raman spectroscopy measurements, an achromatic half-wave plate was placed just before the objective and rotated in steps of 7.5° from 0° to 180°. An analyzing polarizer was placed in front of the spectrometer entrance and kept vertical/horizontal for parallel (*XX*)/perpendicular (*XY*) polarization channels, respectively.

Optical reflection and transmission data were recorded using a stabilized tungsten halogen lamp (Thorlabs SLS201L) and a spectrometer (Thorlabs CCS175). Measurements were performed at room temperature using a single crystal of AgCrP$_2$S$_6$ with thickness ≈100 µm. A 20× objective (Olympus) was used for focusing and collection. For reflection measurements, a broadband plate beam splitter (Thorlabs BSW26) was used at 45° incidence to collect the backscattered signal. Subsequent measurements of the T and R were recorded and used to calculate the absorbance as $A = 1 - T - R$, as shown in Figure 2. All measurements were unpolarized and recorded at normal incidence along the c-axis.

Density Functional Theory Calculations: The electronic structure was calculated using SG15 pseudopotential based on an atomic basis set. The Heyd–Scuseria–Ernzerhof hybrid functional was used to deal with exchange correlation interaction. A k-point mesh of $7 \times 3 \times 1$ was sampled in momentum space. The magnetic exchange interaction was calculated according to the Heisenberg exchange function using Siesta and TB2J. The Perdew–Burke–Ernzerhof + U functional with a plane-wave basis set was used and the U level was varied to reproduce the experimental Néel temperatures of 21 K.[34,35] The magnetic ground state was determined by energy minimization. It was found that $U = 3$ eV gave a reasonable trend of the magnetization versus temperature but the Néel temperature was slightly higher than experimental. Therefore, all exchange coupling values obtained with $U = 3$ eV were reduced by 50% to match the experimental Néel temperature. The single-ion anisotropy term K was calculated by obtaining the energy difference between all spins aligned along the b-direction and along the a- or c-direction. Spin–orbit coupling was included using fully relativistic pseudopotentials and $K = 0.03$ meV.

Atomistic Magnetic Simulation: The following spin Hamiltonian

$$H = \sum_i - K_i \vec{S}_{ib}^2 + \sum_{i \neq j} - J_{ij} \vec{S}_i \cdot \vec{S}_j \tag{1}$$

was used to simulate the Néel temperature using the Vampire atomistic magnetic simulation software,[36] where K_i is the anisotropy term, J_{ij} is the exchange coupling, S_i and S_j are the unit vectors of the spin moment.

Equilibration time steps and averaging time steps were set to 25 000 and 50 000 with a time step increment of 1.

Spin–Spin Correlation Function: The spin–spin correlation function was calculated using the following equal-time correlation function equation

$$C(r) = \left\langle \vec{S}_1(0) \cdot \vec{S}_2(r) \right\rangle - \langle \vec{S}_1(0) \rangle \langle \vec{S}_2(r) \rangle \tag{2}$$

where $\vec{S}_{1,2}$ are the spin vectors and r is the distance. Correlation functions for intrachain, interchain, and interlayer were calculated. The atomic coordinates and spin configurations generated using Vampire simulations were utilized in the correlation function.

The functional form for the fits below the Néel temperature was

$$a \times e^{-\frac{r}{\zeta_{corr}}} + (1-a) \times \cos(\Omega r) \tag{3}$$

and the functional form for the fits above the Néel temperature was

$$e^{-\frac{r}{\zeta_{corr}}} \times \cos(\Omega r) \tag{4}$$

The correlation length was very temperature-dependent and was on the order of a few nanometers to tens of nanometers just above the Néel temperature. This characteristic distance was consistent with the finite system effects on the order of tens of nanometers (and not 100s or 1000s of nanometers).

Magnetic Vector Potential and Ptychographic Reconstructions: Bulk and surface magnetizations were constructed by placing (canted) spin dipoles on Cr sites using kernel density estimation. The magnetic vector potential was then constructed by convolving the bulk and surface magnetizations with the model spin orientations according to

$$A \propto \frac{\hat{\mu} \times r}{r^3} M(r) \tag{5}$$

where A is the magnetic vector potential, $\hat{\mu}$ is the bulk/surface-spin orientation, and $M(r)$ is the bulk/surface magnetization evaluated at position r.

Electrostatic and magnetic vector potential contributions were simulated using multislice formalism, as implemented in the open-source software abTEM,[37] with the same accelerating voltage and convergence semiangle as above, albeit using a defocus value of 200 Å and a finite electron-dose of 1×10^6 e$^-$ Å^{-2}.

Simultaneous ptychographic reconstructions were performed using the formalism introduced in ref. [29], as implemented in the open-source software py4DSTEM,[38] using 1.0 Å^{-1} Butterworth filtering of the magnetic vector potential.

Theory for Twisted Magnets: This was started by writing down the energy function for the magnetization considering a single chain in the top layer, rotated from the lab frame with angle $+\vartheta/2$, and a single chain in the bottom layer, rotated with respect to the lab frame with angle $-\vartheta/2$. This is shown in the schematic diagram in Figure 4f.

In this configuration, the easy axis in each layer is given in the lab frame by

$$\mathbf{n}\left(\pm\frac{\vartheta}{2}\right) = \mp\sin\left(\frac{\vartheta}{2}\right)\mathbf{e_x} + \cos\left(\frac{\vartheta}{2}\right)\mathbf{e_y} \tag{6}$$

with the signs chosen for their respective layers.

For simplicity, a single site was focused on, which was assumed to lie at the intersection of the two chains, where the effect was expected to be maximal. In this case, the energy can be written as a sum

$$E = E_{top} + E_{bottom} + E_{inter} \tag{7}$$

with

$$E_{top} = -K\left(S_t \cdot n\left(\frac{\vartheta}{2}\right)\right)^2 + 2J_{\parallel}S_t \cdot n\left(\frac{\vartheta}{2}\right) \tag{8}$$

$$E_{bottom} = -K(S_b \cdot n(-\vartheta/2))^2 + 2J_{\parallel}S_b \cdot n(-\vartheta/2) \tag{9}$$

$$E_{inter} = J_{\perp}S_b \cdot S_t \tag{10}$$

Here, $K > 0$ is the easy-axis anisotropy, which favored the spin to lie perpendicular to the chain axis, $J_{\parallel} > 0$ is the intralayer antiferromagnetic coupling, which favored the spin to antialign with its neighbors in the same chain, and $J_{\perp} > 0$ is the interchain exchange coupling, which was taken here to be ferromagnetic. For estimates of the values, DFT + U calculations, combined with TB2J calculations of the magnetic exchange parameters (Experimental Section) were relied upon, with $K = 0.03$ meV, $J_{\parallel} = 3.91$ meV, and $J_{\perp} = 0.186$ meV.

Supporting Information

Supporting Information is available from the Wiley Online Library or from the author.

Acknowledgements

Conflict of Interest

The authors declare no conflict of interest.

Author Contributions

E.P. and F.M.R. conceived the idea and directed the project. K.M. and Z.S. performed crystal growth of the bulk material. E.P. fabricated TEM samples

Data Availability Statement

The data that support the findings of this study are available in the Supporting Information of this article.

Keywords

1D magnetism, 2D magnets, 2D materials, scanning transmission electron microscopy

[1] C. Ruegg, N. Cavadini, A. Furrer, H.-U. Güdel, K. Krämer, H. Mutka, A. Wildes, K. Habicht, P. Vorderwisch, *Nature* **2003**, *423*, 62.

[2] T. Giamarchi, C. Uegg, O. Tchernyshyov, *Nat. Phys.* **2003**, *4*, 198.

[3] J. Zhang, X. Wang, L. Zhou, G. Liu, D. T. Adroja, I. da Silva, F. Demmel, D. Khalyavin, J. Sannigrahi, H. S. Nair, L. Duan, J. Zhao, Z. Deng, R. Yu, X. Shen, R. Yu, H. Zhao, J. Zhao, Y. Long, Z. Hu, H.-J. Lin, T.-S. Chan, C.-T. Chen, W. Wu, C. Jin, *Adv. Mater.* **2022**, *34*, 2106728.

[4] Y. Ueda, *Chem. Mater.* **2004**, *10*, 2653.

[5] H. Roder, E. Hahn, H. Brune, J. B. Ie, K. Kern, *Nature* **1993**, *366*, 141.

[6] P. Gambardella, A. Dallmeyer, K. Maiti, M. C. Malagoli, W. Eberhardt, K. Kern, C. Carbone, *Nature* **2002**, *416*, 301.

[7] S. Loth, S. Baumann, C. P. Lutz, D. M. Eigler, A. J. Heinrich, *Science* **2012**, *335*, 196.

[8] C. F. Hirjibehedin, C. P. Lutz, A. J. Heinrich, *Science* **2006**, *312*, 1021.

[9] A. A. Khajetoorians, J. Wiebe, B. Chilian, R. Wiesendanger, *Science* **2011**, *332*, 1062.

[10] K. S. Burch, D. Mandrus, J. G. Park, *Nature* **2018**, *563*, 47.

[11] B. Huang, M. A. McGuire, A. F. May, D. Xiao, P. Jarillo-Herrero, X. Xu, *Nat. Mater.* **2020**, *19*, 1276.

[12] A. Allain, J. Kang, K. Banerjee, A. Kis, *Nat. Mater.* **2015**, *14*, 1195.

[13] S.-H. Bae, H. Kum, W. Kong, Y. Kim, C. Choi, B. Lee, P. Lin, Y. Park, J. Kim, *Nat. Mater.* **2019**, *18*, 550.

[14] H. Mutka, C. Payen, P. Molinié, *Europhys. Lett.* **1993**, *21*, 623.

[15] S. Selter, Y. Shemerliuk, B. Buchner, S. Aswartham, *Crystals* **2021**, *11*, 500.

[16] H. Mutka, J. L. Soubeyroux, G. Bourleaux, P. Colombet, *Phys. Rev. B* **1989**, *39*, 4820.

[17] F. D. M. Haldane, *Phys. Rev. Lett.* **1983**, *50*, 1153.

[18] G. Long, H. Henck, M. Gibertini, D. Dumcenco, Z. Wang, T. Taniguchi, K. Watanabe, E. Giannini, A. F. Morpurgo, *Nano Lett.* **2020**, *20*, 2452.

[19] A. R. Wildes, V. Simonet, E. Ressouche, G. J. McIntyre, M. Avdeev, E. Suard, S. A. J. Kimber, D. Lançon, G. Pepe, B. Moubaraki, T. J. Hicks, *Phys. Rev. B* **2015**, *92*, 224408.

[20] Y. Shemerliuk, Y. Zhou, Z. Yang, G. Cao, A. U. B. Wolter, B. Büchner, S. Aswartham, *Electron. Mater.* **2021**, *2*, 284.

[21] X. He, N. Helbig, M. J. Verstraete, E. Bousquet, *Comput. Phys. Commun.* **2021**, *264*, 107938.

[22] J. M. Soler, E. Artacho, J. D. Gale, A. García, J. Junquera, P. Ordejón, D. Sánchez-Portal, *J. Phys.: Condens. Matter* **2021**, *14*, 2745.

[23] D. Lancon, R. A. Ewings, T. Guidi, F. Formisano, A. R. Wildes, *Phys. Rev. B* **2021**, *97*, 134414.

[24] J. Klein, T. Pham, J. D. Thomsen, J. B. Curtis, T. Denneulin, M. Lorke, M. Lorke, M. Florian, A. Steinhoff, R. A. Wiscons, J. Luxa, Z. Sofer, F. Jahnke, P. Narang, F. M. Ross, *Nat. Commun.* **2022**, *13*, 5420.

[25] E. Lieb, D. Mattice, *J. MJath. Phys.* **1962**, *3*, 749.

[26] D. Maiti, D. Dey, M. Kumar, *Condens. Matter* **2023**, *8*, 17.

[27] N. Fujiwara, M. Hagiwara, *Solid State Commun.* **2000**, *113*, 433.

[28] S. F. Weber, A. Urru, S. Bhowal, C. Ederer, N. A. Spaldin, *Physical Review X* **2024**, *14*, 021033 .

[29] G. Varnavides, S. Ribet, R. Yalisove, J. Moore, C. Ophus, M. C. Scott, *Microsc. Microanal.* **2023**, *29*, 278.

[30] T. Song, Q.-C. Sun, E. Anderson, C. Wang, J. Qian, T. Taniguchi, K. Watanabe, M. A. McGuire, R. Stöhr, D. Xiao, T. Cao, J. Wrachtrup, X. Xu, *Science* **2021**, *374*, 1140.

[31] B. Lake, D. A. Tennant, C. D. Frost, S. E. Nagler, *Nat. Mater.* **2005**, *4*, 329.

[32] Q. Wang, M. Kewenig, M. Schneider, R. Verba, F. Kohl, B. Heinz, M. Geilen, M. Mohseni, B. Lägel, F. Ciubotaru, C. Adelmann, C. Dubs, S. D. Cotofana, O. V. Dobrovolskiy, T. Brächer, P. Pirro, A. V. Chumak, *Nat. Electron.* **2020**, *3*, 765.

[33] X.-Y. Wei, O. A. Santos, C. H. S. Lusero, G. E. W. Bauer, J. Ben Youssef, B. J. van Wees, *Nat. Mater.* **2022**, *21*, 1352.

[34] J. P. Perdew, K. Burke, M. Ernzerhof, *Phys. Rev. Lett.* **1996**, *77*, 3865.

[35] S. L. Dudarev, G. A. Botton, S. Y. Savrasov, C. J. Humphreys, A. P. Sutton, *Phys. Rev. B* **1998**, *57*, 1505.

[36] R. F. L. Evans, W. J. Fan, P. Chureemart, T. A. Ostler, M. O. A. Ellis, R. W. Chantrell, *J. Phys. Condens. Matter* **2014**, *26*, 10.

[37] J. Madsen, T. Susi, *Open Res. Europe* **2021**, *1*, 24.

[38] G. Varnavides, S. M. Ribet, S. E. Zeltmann, Y. Yu, B. H. Savitzky, D. O. Byrne, F. I. Allen, V. P. David, M. C. Scott, C. Ophus, *arXiv:2309.05250* **2023**.

2401534 (9 of 9)